

SUPPORTING INFORMATION FOR

Modeling, Simulation, and Design Criteria for Photoelectrochemical Water-Splitting Systems

Sophia Haussener, Chengxiang Xiang, Josh M. Spurgeon,

Shane Ardo, Nathan S. Lewis, and Adam Z. Weber

Hydrogen crossover and safety

An approximate mass-balance calculation for an open system at generation current densities of 20 mA cm^{-2} is shown in Figure S1. The hydrogen concentration in the anode side, which contains oxygen and inert sweep gas, is given by,

$$c_{\text{H}_2} = \frac{N_{\text{H}_2,\text{x}}}{N_{\text{O}_2} + N_{\text{sweep}}} = \frac{i_{\text{R}}(1 - \eta)/(2F)}{i_{\text{R}}/(4F) + N_{\text{sweep}}}, \quad (\text{S1})$$

where subscript x denotes crossover fluxes. Oxygen crossover is assumed to be negligible, and gas accumulation in the head space has been neglected.

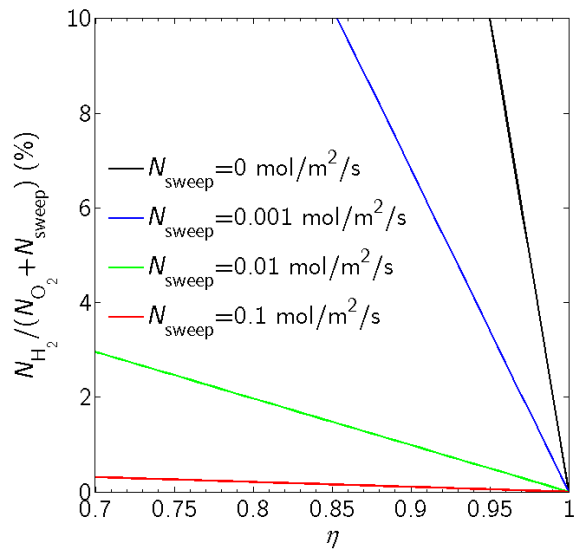


Figure S1 –Hydrogen concentration at the anode side, as a function of current efficiency, for different sweep gas molar fluxes at an applied current density of 20 mA cm^{-2} .

Structure–property relations

Permeability - A second permeability formulation for the permeable porous separators, representing a more structured, fibrous-like morphology, is given by

$$K_{\text{fib}} = \frac{\varepsilon^3 d^2}{36 \cdot 1/2 (k_{\perp} + k_{\parallel}) \cdot (1 - \varepsilon)^2}, \quad (\text{S2})$$

where k_{\perp} and k_{\parallel} represent the Kozeny constants for flow around perpendicular or parallel arranged cylinders, respectively^{1,2}:

$$k_{\perp} = \frac{\frac{2\varepsilon^3}{1-\varepsilon}}{\frac{1}{1-\varepsilon} - \frac{1-(1-\varepsilon)^2}{1+(1-\varepsilon)^2}}, \quad (\text{S3})$$

$$k_{\parallel} = \frac{2\varepsilon^3}{(1-\varepsilon)(2\ln(1/(1-\varepsilon))-3+4(1-\varepsilon)-(1-\varepsilon)^2)}. \quad (\text{S4})$$

Conductivity - The conductivity is also affected by the morphology of the separator. An approach that has been used previously to evaluate the morphology-dependent thermal conductivity was used herein to represent a more structured, fibrous-like morphology. A combination of liquid and solid structures were arranged parallel or perpendicular to the potential³, as given by

$$\kappa_{l,e,\text{fib}} = \kappa_l \left(0.5 \cdot \frac{\sigma_s}{\kappa_l} \left(\varepsilon \frac{\kappa_l}{\sigma_s} + 1 - \varepsilon \right) + 0.5 \cdot \frac{1}{\varepsilon \left(1 - \frac{\kappa_l}{\sigma_s} \right) + \frac{\kappa_l}{\sigma_s}} \right). \quad (\text{S5})$$

κ_l/σ_s was chosen to be 10^4 , a value for which the morphology dominates the conductivity, rather than the ratio of the single phase conductivities.

Figure S2 shows the values for the two permeability and conductivity formulations as a function of the porosity and characteristic pore dimension of the separator. The morphology dependence of the diffusion coefficient in the separator has been neglected (Bruggeman relation, Eq. 18 for diffusivity, is used), as crossover is dominated by convection for the fibrous separator.

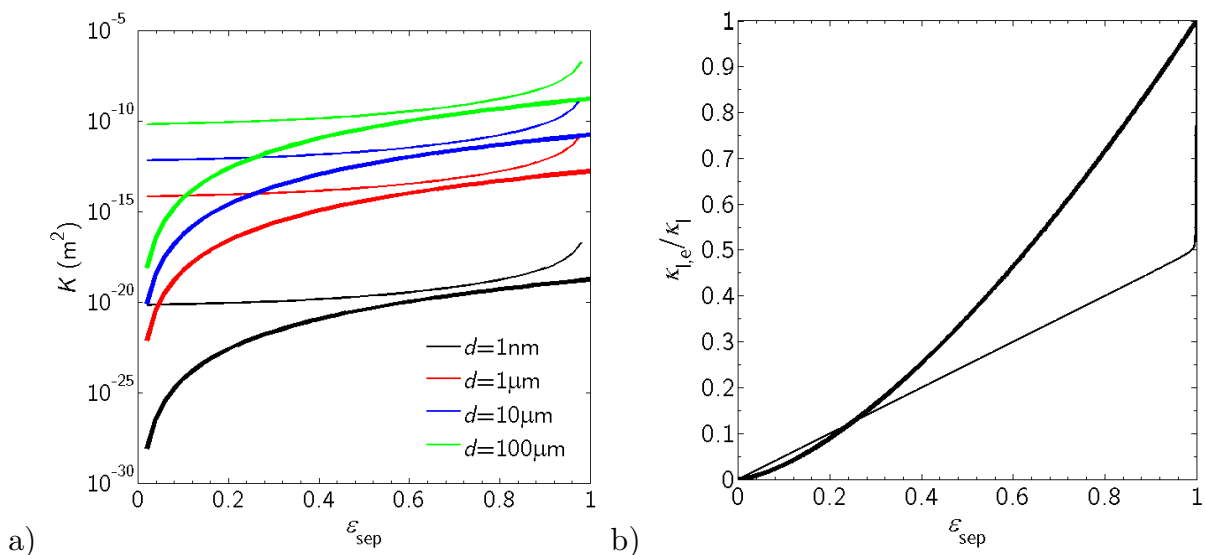


Figure S2 – Permeability (a) and conductivity (b) as a function of porosity for a structured, fibrous-like separator (thin lines), Eq. S2 and Eq. S5, respectively, and for a packed-bed-like separator (thick lines), Eq. 19 and Eq. 18, respectively.

Model convergence, computational mesh, and solver settings

Mesh and iteration convergence studies were conducted for both designs and all dimensions. Figure S3 depicts an exemplary study for the electrolyte potential in design B for $t_{\text{sep}} = 10 \mu\text{m}$, $l_{\text{el}} = 10 \text{ mm}$, $h_{\text{e}} = 10 \text{ mm}$, and $l_{\text{el}}/l_{\text{d}} = 0.5$.

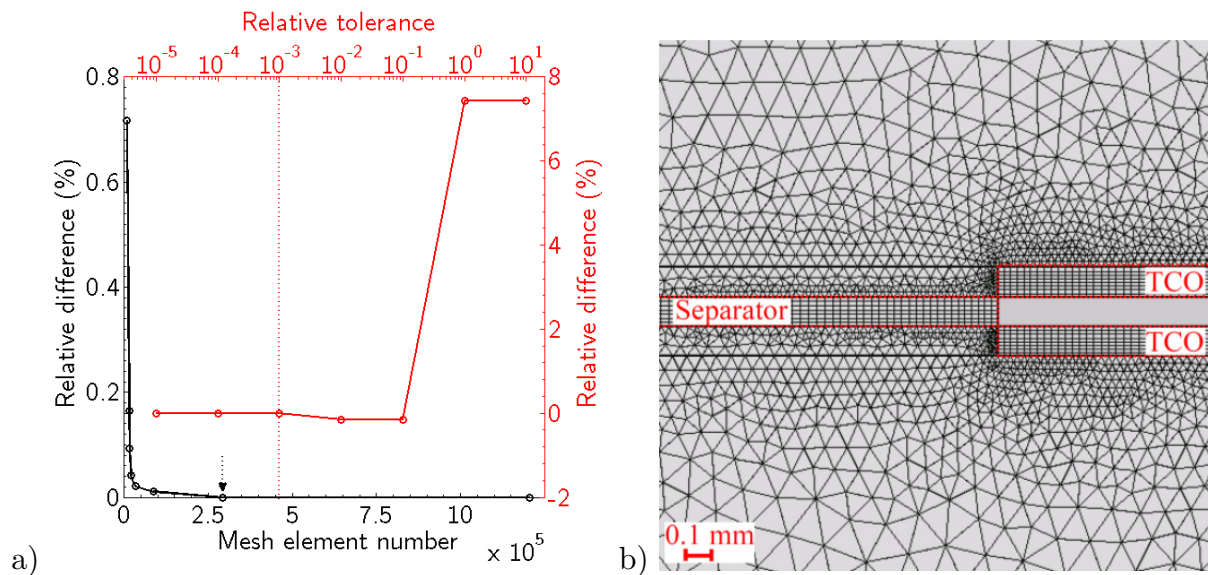


Figure S3 – (a) Relative difference in mean solution potential (vs. ground at the cathode) for varying mesh element numbers and relative iteration tolerance, with the tolerance used in the manuscript indicated by the vertical dotted line, and (b) close-up of mesh with $3 \cdot 10^5$ elements (indicated by arrow in (a)) for design B with $t_{\text{sep}} = 10 \mu\text{m}$, $l_{\text{el}} = 10 \text{ mm}$, $h_{\text{e}} = 10 \text{ mm}$, and $l_{\text{el}}/l_{\text{d}} = 0.5$.

The solution converged with increasing mesh element numbers and decreasing relative iteration tolerance. The chosen convergence criteria for relative tolerance of 10^{-3} is indicated in the figure by the vertical dotted line. The mesh was created by predefining quadrilateral elements in the small separator and TCO components, which defined the triangular elements in the electrolyte, which were also limited to a maximal mesh element size (40 x the smallest element size) and a growth rate of 1.2. These meshes exhibited mean element qualities larger than 0.85.

For computation convergence, direct solvers were chosen: multifrontal massively parallel sparse direct solver (MUMPS) for charge conservation, and parallel sparse direct linear solver (PARADISO) for species, mass, and momentum conservation. Automated damping options with small initial and minimal damping factor were used in the direct solvers and allowed for relatively fast convergence.

Model Validation

Galvanodynamic electrochemical-impedance spectroscopy was used to compare the device physics modeled solution resistances to those observed experimentally in an electrochemical test device. The test device consisted of two platinum wires (diameter 0.5 mm) arranged back-to-back and electrically insulated from one another. The wires were embedded into a circular Teflon platelet (thickness 3.6 mm and diameter d_{Teflon}), as depicted in Figure S4. The Pt–Teflon assembly (electrode) was immersed in a beaker (diameter 10 cm) that contained 1 liter of H_2SO_4 (aq) of various molarities and conductivities (as measured by a conductivity probe). A constant current density of 20 mA/cm² was applied between the front and the backside of the Teflon-embedded Pt wires. The resistance measured by impedance spectroscopy (at 10 μA amplitude) at high frequencies (7 MHz) corresponded to the solution resistance, and was converted to a potential drop using Ohm's law. The measured and calculated solution resistance for three different electrode diameters ($d_{\text{Teflon}} = 1, 3, \text{ and } 5 \text{ cm}$), for 0.09 M – 1.2 M electrolyte, are depicted in Figure S4. Two sets of each electrode were prepared and each measurement was performed three times per electrode, except at the lowest concentration, where only one measurement per electrode was performed. The y-error bars depict the standard deviation of the three measurements per electrode set for each electrode size, in the

specific electrolyte. The relatively large variations between the measurements done with the two different electrode sets were attributed to fabrication differences causing variations in contact resistance within the electrode assembly, additional series resistances (e.g. due to surface impurities and imperfections), and slightly confined current lines due to not perfectly planar Pt-Teflon assembly surfaces. The latter describes the increase of the absolute difference with decreasing solution conductivity, especially because small variations in the experimental conditions are amplified at lower solution conductivity. The relative variation in solution resistance for each size electrode was below 25%. The x-error bars account for variations in the experimental precision (conductivity). The upper and lower dotted lines show the simulated minimal and maximal solution resistance, respectively, and the solid lines show the simulated mean solution resistance. The simulated results for the three different electrode diameters almost overlay.

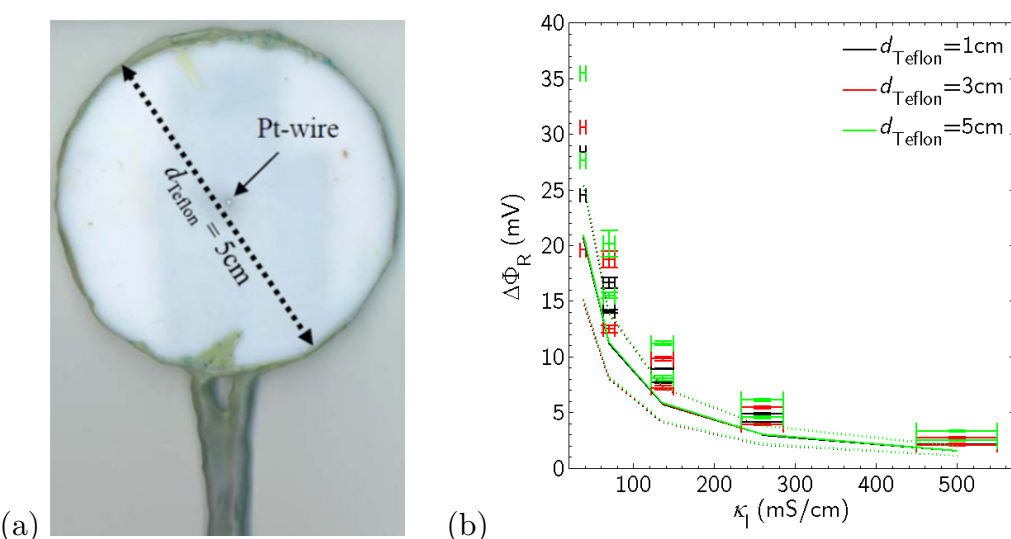


Figure S4 – (a) Digital photograph of one side of the Pt-Teflon-assembly used for the electrochemical-impedance-spectroscopy measurements. The other side was identical. (b) Measured (symbols) and calculated (mean: solid line, min and max: dotted lines) potential losses in the solution for the three different Teflon platelet sizes and the two sets of electrodes, as a function of the conductivity of the solution.

The systematic underprediction of the solution resistance by the simulations is mainly associated with imprecise calibration of the conductivity probe, and imperfections in the experimental systems that are not accounted for in the

simulations, e.g. additional contact and series resistances within and at the surface of the electrode.

Potential distributions

The cathode potential distributions in the electrolyte are shown in Figure S5, for design A and design B, respectiviely, for exemplary component dimensions.

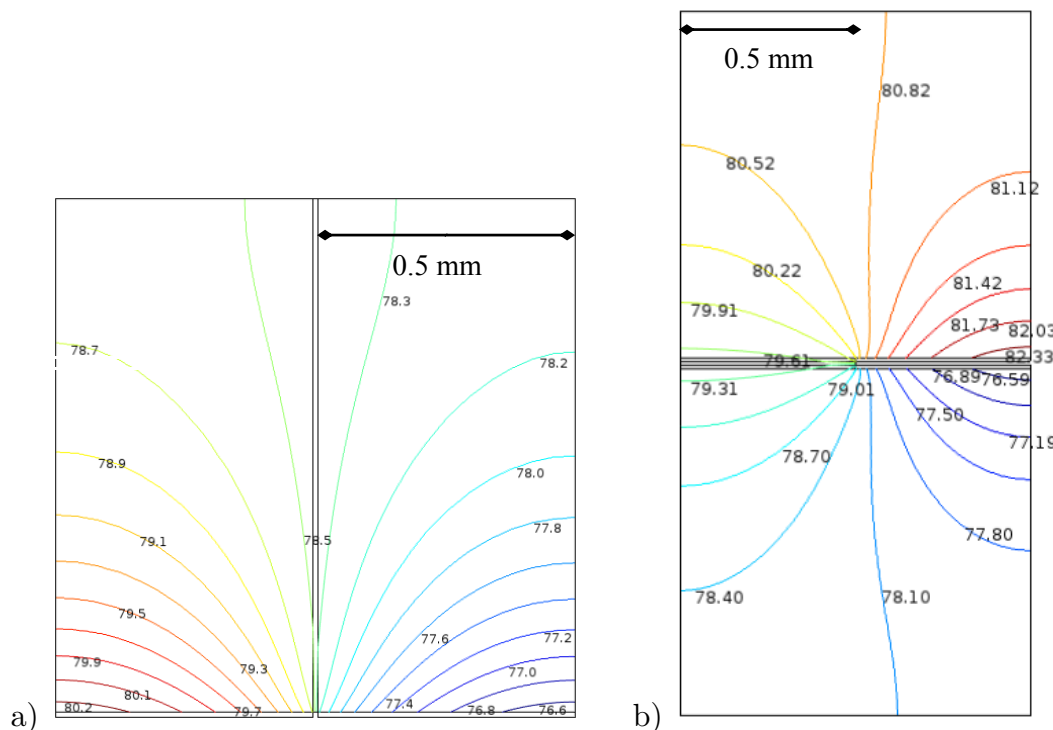


Figure S5 – Electrolyte potential (vs. ground at the cathode, in mV) for (a) design A, $t_{\text{sep}} = 10 \mu\text{m}$, $l_{\text{el}} = 1 \text{ mm}$, $h_{\text{e}} = 1 \text{ mm}$, and for (b) design B, $t_{\text{sep}} = 10 \mu\text{m}$, $l_{\text{el}} = 1 \text{ mm}$, $h_{\text{e}} = 1 \text{ mm}$, and $l_{\text{el}}/l_{\text{d}} = 0.5$. The separator is represented by the rectangular domain in the center (design A: vertical, design B: horizontal, left side), separating the anode (design A: left bottom, design B: middle, top right) and cathode (design A: right bottom, design B: middle, bottom right) side. The TCOs are represented by the rectangular domains at the bottom of the anode and cathode sides for design A, and at the top and bottom of the PV/separator on the right side for design B.

Structure–property influence

The results of the simulations using the fibrous (Eqs. S2 and S6), instead of packed bed (Eqs. 19 and 18), treatment of the permeability and conductivity of the separator are shown in Figures S6 and S7, respectively, for designs A and B.

Compared to the random, packed-bed-like structure, the fibrous structure allows for lower hydrogen collection yields at the same separator porosities, or for the use of less permeable materials to obtain the same efficiency as a packed-bed-like material at this porosity. On the other hand, the ohmic losses of a system using a fibrous-like separator are smaller, for smaller ε_{sep} , compared to the packed bed-like separator material. Nevertheless, this advantage is lost at $\varepsilon_{\text{sep}} > 0.3$, as the packed bed's $\kappa_{l,e}$ becomes larger than fibrous bed's $\kappa_{l,e}$ at the same porosity (see Figure S2).

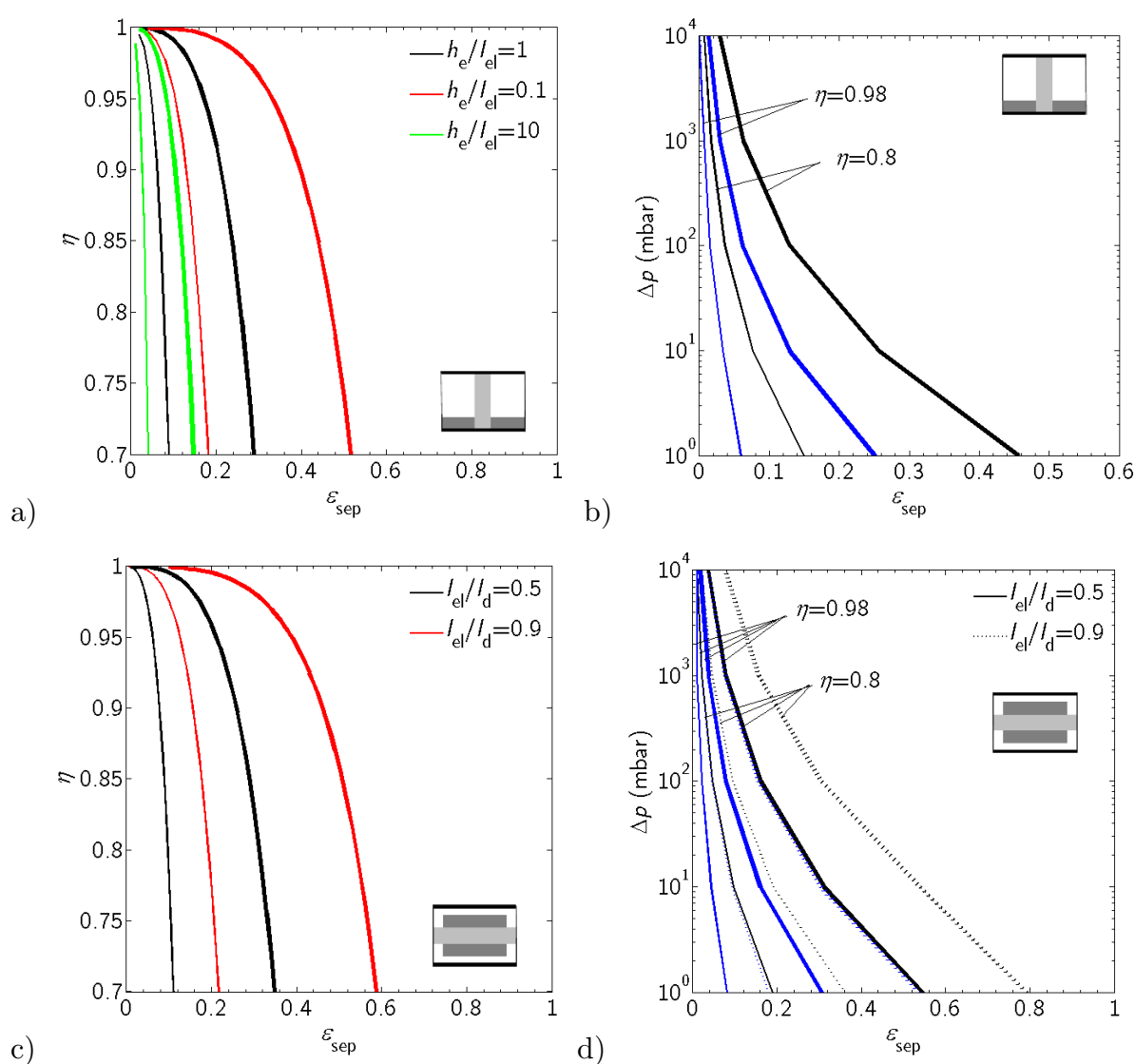


Figure S6 – (a,c) Hydrogen collection yield at $\Delta p = 10 \text{ mbar}$, as a function of separator porosity, at $t_{\text{sep}} = 10 \mu\text{m}$ (thin lines) and $t_{\text{sep}} = 500 \mu\text{m}$ (thick lines) for the indicated component dimensions in design A (a), and for $h_e = 1 \text{ mm}$ and $l_{\text{el}} = 1 \text{ mm}$ in design B (c). (b,d) Differential pressure at $\eta = 0.8$ (black) and 0.98 (blue) as a function of separator porosity, at $t_{\text{sep}} = 10 \mu\text{m}$ (thin lines) and $t_{\text{sep}} = 500 \mu\text{m}$ (thick lines) for $h_e = 1 \text{ mm}$ and $l_{\text{el}} = 1 \text{ mm}$ in design A (b), and design B (d).

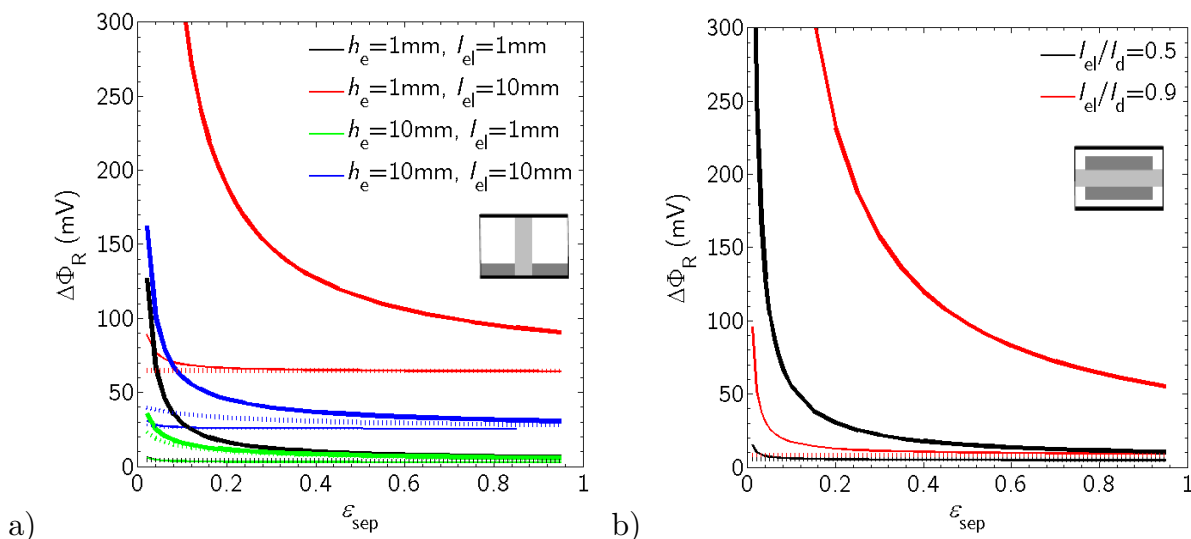


Figure S7 – Average ohmic potential drop (solid line) and average ohmic potential drop minus the average potential drop over the membrane (dotted line), as a function of separator porosity, for $t_{sm} = 10\mu\text{m}$ (thin lines) and $t_{sep} = 500\mu\text{m}$ (thick lines), for various dimensions of design A (a), and design B at $h_e = 1\text{ mm}$ and $l_{el} = 1\text{ mm}$ (b).

References

- 1 E. Sparrow and A. Loeffler, *American Institute of Chemical Engineers*, 1959, **5**, 325–330.
- 2 S. Kuwabara, *Journal of Physical Society of Japan*, 1959, **14**, 527–532.
- 3 S. Haussener, *Transport phenomena in complex multi-phase media. A tomography-based approach applied to solar fuel production and snow science*, SVH Südwestdeutscher Verlag für Hochschulschriften, 2012.